

Impedance characteristics under different voltages of *n*- β -FeSi₂/*p*-Si heterojunctions constructed via facing target sputtering

Nattakorn Borwornpornmetee^a, Rawiwan Chaleawpong^a, Peerasil Charoenyuenyao^a, Adison Nopparuchikun^a, Boonchoat Paosawatyanyong^b, Phongsaphak Sittimart^c, Tsuyoshi Yoshitake^c, Nathaporn Promros^{a,*}

^a Department of Physics, School of Science, King Mongkut's Institute of Technology Ladkrabang, Ladkrabang, 10520, Bangkok, Thailand

^b Department of Physics, Faculty of Science, Chulalongkorn University, Pathumwan, 10330, Bangkok, Thailand

^c Department of Advanced Energy Science and Engineering, Kyushu University, Kasuga, 816-8580, Fukuoka, Japan



ARTICLE INFO

Keywords:

n- β -FeSi₂/*p*-silicon heterojunctions

Impedance characteristics

Circuit parameters

Carrier relaxation time

Electrical conductivities

ABSTRACT

Utilizing a substrate temperature of 600 °C, *n*-semiconducting iron disilicide (β -FeSi₂)/*p*-silicon heterojunctions have been constructed with direct-current sputtering and a couple of facing FeSi₂ targets. The impedance examination was carried out under a voltage ranging from -1 V to 1 V. Each complex impedance arch unveiled only one arc with its center beneath the real axis. Elevated voltage facilitates a reduction in the semicircle size. Based on the simulated equivalent circuit model, the heterojunctions possessed high parallel resistance and a constant phase element (CPE) at the grain boundary, raising the *V*. The CPE for the grain, grain boundary, and junction implied behavior close to the ideal capacitor. The dielectric loss tangent results indicated that the heterojunctions exhibited leakage behavior. From the alternating-current conductivity plots, the plateau and dispersion areas were revealed at low and high frequencies, respectively. The direct-current conductivity was 9.49×10^{-3} S cm⁻¹ at -1 V and elevated to 8.87×10^{-2} S cm⁻¹ at 1 V, due to the augmented charge carriers. Jonscher's power law fitting exposed that the constructed heterojunction exhibited short-range hopping within the boundary of the neighborhood.

1. Introduction

Based on worldwide reports, the semiconducting variant of iron disilicide with an orthorhombic form (β -FeSi₂) has attracted significant interest in recent years for incorporation with Si technology applied in near-infrared (NIR) photodetectors due to the plausible ability of its physical attributes [1,2]. β -FeSi₂ material is manufactured from natural, abundant, and non-harmful substances of iron (Fe) and silicon (Si), which make up 5% and 26% of the Earth's crust, respectively [2,3]. Epitaxial β -FeSi₂ films on Si wafers were also achieved with 2–5% of the lattice-mismatched value [4]. β -FeSi₂ films possess many outstanding optical attributes such as 0.76 eV of an indirect optical bandgap and 0.85 eV of a direct optical bandgap [5], as well as an absorption coefficient higher than 10^5 cm⁻¹ for the 1.2 eV photon energy, all of which are considerable attributes for an optoelectronic material [5,6]. Various film-coating processes have been successfully employed to coat β -FeSi₂ films [7–9]. However, the post-annealing dependence of such processes

contributes to the Fe diffusion onto the Si layer, resulting in deep trap levels [10–12]. Hereupon, the β -FeSi₂ films coated under lower temperatures, are preferable.

Primarily, direct-current sputtering (DCS) with a couple of facing targets is employed for coating magnetic material such as Fe₃Si [13]. It is appropriate for coating high-quality β -FeSi₂ films because of the low-temperature manufacturing process [14,15]. Due to DCS having a pair of facing targets, β -FeSi₂ films could be epitaxially constructed onto Si(111) wafers without thermal annealing using a substrate temperature of 600 °C in early research [16]. The β -FeSi₂ films manufactured using the Si(111) wafer as a substrate exposed the conduction in an *n*-semiconductor [17]. The carrier densities of the *n*- β -FeSi₂ films and *p*-Si wafers investigated under a temperature of 300 K were individually found to be roughly 1.0×10^{17} cm⁻³ and 1.5×10^{15} cm⁻³ [18]. Previously, we investigated the structural properties of β -FeSi₂ under varying substrate temperatures of 525, 550, 600, and 660 °C [6,12]. All β -FeSi₂ films under a substrate temperature of 600 °C consisted of

* Corresponding author.

E-mail address: nathaporn_promros@kyudai.jp (N. Promros).

poly-crystalline. Epitaxial growth of β -FeSi₂ films on Si(111) wafers at a substrate temperature of 600 °C or higher was found. The crystallinity of β -FeSi₂ films was enhanced at a substrate temperature of 660 °C [6,12]. More importantly, we investigated the current-voltage (I - V) characteristics in the darkness of the n - β -FeSi₂/ p -Si heterojunctions, with the β -FeSi₂ films deposited at different substrate temperatures of 525, 550, 600, and 660 °C [6]. We found that the β -FeSi₂/Si heterojunctions prepared at a substrate temperature of 600 °C exhibited good rectifying properties together with a lower leakage current in comparison with another one. In contrast, the β -FeSi₂/Si heterojunctions prepared at substrate temperatures of less or more than 600 °C showed poor rectifying properties together with a large leakage current [6]. Although, the β -FeSi₂ films deposited at a substrate temperature of 660 °C showed better crystallinity than those prepared at a substrate temperature of 600 °C, their I - V characteristics were degraded. This could be attributable to the increment in the concentration of Fe atoms that diffused into the depletion region being expanded in the Si wafer side. The diffused Fe atoms form deep energy levels, thereby increasing the leakage current [12]. Based on the obtained results, a substrate temperature of 600 °C is the optimum point suitable for photodiode and photovoltaic application.

In our previous studies, the n - β -FeSi₂/ p -Si heterojunctions and the Ohmic metallic contacts were manufactured and employed to detect NIR light [17,18]. The manufactured heterojunction devices presented good rectifying action and response under the illumination of NIR light [17, 18]. Based on the results of conductance and capacitance extracted against different voltages (V) and frequencies (f) in the dark, the interface state density and series resistance (R_s) for the manufactured heterojunctions were computed as a function of the f value via the Hill-Coleman and Nicollian-Brews methods used in our previous research [18]. However, further study is required regarding the impedance characteristics, equivalent circuit modeling, assessment of relaxation time of carrier (τ), circuit parameters, conductivity under alternating-current (σ_{AC}), conductivity under direct-current (σ_{DC}), inclusive mechanisms of the carrier's movement, polarization, and relaxation of the n - β -FeSi₂/ p -Si heterojunctions manufactured via DCS along with a couple of facing targets to provide greater understanding.

The well-established impedance spectroscopy approach is used to investigate the electrical attributes of solid-state devices in various forms, such as photovoltaic cells, optoelectronics, and heterojunctions [19–24]. The administration of impedance spectroscopy can result in the characterization of electrical properties on semiconductor devices, where the small AC signal excited with a broad f is utilized [19,20]. The comprehensible result of the complex impedance ($Z(\omega)$) is usually represented via the arcs of real Z' versus imaginary Z'' , which can be captured through the sinusoidal signal response of the devices and employed to interpret the occurring electrical phenomena of the semiconductor devices [19–24]. The semicircular arcs of Z'' - Z' can also form the basis of an equivalent circuit, composed of resistors, capacitors, or inductors, representing the characteristics of the heterojunctions in relation to the biased signal [19–21]. The dielectric characteristics can be roughly calculated using impedance characteristics. Complex permittivity ($\epsilon(\omega)$) of the heterojunctions, divided into the real term (ϵ') and imaginary term (ϵ''), as well as the tangent of dielectric loss ($\tan \delta$), can be used to study the behavior of the polarization and relaxation on the heterojunctions [25–27]. Hence, dielectric characteristics featured alongside impedance spectroscopy result in several pieces of literature from other research groups [28–30]. Likewise, the extraction of σ_{AC} profiles can also be provided utilizing the impedance data [31]. Typically, the σ_{AC} outcomes can be applied to delineate the significant data about the main conduction models compatible with the materials, determined as the variable range hopping model and band theory [32, 33]. The f dependence of the σ_{AC} characteristics also invokes information on the processes of charge transfer on semiconductor materials and identifies their primary conduction and relaxation process [34,35]. Besides, the σ_{AC} characteristics at a high f regime can forecast the behavior

of the charge carrier during relaxation and the jump relaxation model (JRM) [35,36]. The assessment of σ_{DC} can be achieved using the y-axis interception drawn through the flat region at a low f zone of the plot between σ_{AC} and f [35]. The mechanism behind electrical conduction and the electrical charge transfer associated with the devices can be interpreted through the σ_{DC} aspect [32,35]. For these reasons, dielectric and conduction properties are also reported as valuable assets for this study on the mechanism of manufactured heterojunctions.

Under the investigation of impedance characteristics with the condition of alternating-current V change, an increase in V results in a decrease in the depletion region width due to the drift field having less exposure to the active layer [20]. Following the shrinkage of the depletion region, carrier recombination and charge carrier transfer due to electrical injections become more viable, increasing the current density as the resistance weakens with the increasing V [37–39]. At the same time, the charge carriers are amassed at the interfaces between the charge transport layer and the active layer, increasing the capacitance with increasing V [19]. Additionally, an increase in the biased signal can induce a change in conductivity since the rise in charge carriers within the materials and the change in dielectric properties due to the rise in the field need to be absorbed [30,35]. Therefore, the experiments performed under a variation of V would be suitable for extracting precise results on the change of impedance and associated electrical properties in response to the biased signal [40]. Consequently, this scenario focuses on the electrical characteristics of n - β -FeSi₂/ p -Si heterojunction devices created via DCS along with a couple of facing targets. These are examined under various V values at room temperature, such as the study of impedance characteristics, estimation of τ value, anticipation of an equivalent circuit model, extraction of circuit parameters, exploration of σ_{AC} and σ_{DC} , in addition to the elucidations of the carrier portage behavior, carrier relaxation phenomenon, conduction process, and JRM for the constructed heterojunctions. Based on our knowledge, these parameters of n - β -FeSi₂/ p -Si heterojunction were originally reported in this research to clarify the equivalent circuit characteristics, dielectric properties, and charge transport mechanism of the heterojunctions under various bias voltages.

2. Experimental section

2.1. Creation of heterojunction consisting of p -Si wafer and n - β -FeSi₂ film

The n - β -FeSi₂/ p -Si heterojunctions were constructed through the DCS apparatus with a pair of facing targets, where a pair of FeSi₂ targets with 4 N purity (supplied by Toshima Manufacturing Co., Ltd.) was used to coat the β -FeSi₂ layer. The substrate for coating the β -FeSi₂ films was a 260 μm -thick p -Si(111) wafer with a resistivity of 10–20 $\Omega \cdot \text{cm}$. By employing an ultrasonicator (Branson 2510 supplied by Yamato Scientific Co., Ltd.), the Si wafer was cleansed in acetone and methanol with 2 N purity (supplied by FUJIFILM Wako Pure Chemical Corporation) as well as deionized (DI) water. The rinsing process was performed in a beaker placed in an ultrasonic cleaner, with each rinsing step lasting 5 min. During this Si cleaning process, solvents such as acetone and methanol were utilized to wipe off any organic remains, including oils. Additionally, DI water was employed to remove the remaining solvent. The 1% diluted hydrofluoric (HF) solvent (supplied by Morita Chemical Industries Co. Ltd.) was applied for the clearance of residual oxide contaminant on the Si(111) wafer's surface. The excess HF left behind after the oxide removal was rinsed with DI water, and the Si wafer substrate then thoroughly blown by nitrogen (N_2) gas with 5 N purity (supplied by Iwatani Corporation) to eliminate humidity.

For the β -FeSi₂ film sputtering, the cleaned Si wafer was transferred to the cleanroom and placed on a holder at a fixed 7.5 cm distance away from the β -FeSi₂ targets in the DCS apparatus with a pair of facing targets. The CIT-Alcatel 2030C Rotary Vane Vacuum Pump (supplied by Alcatel Japan)/Osaka Vacuum TG1300 Compound Turbo Molecular Pump (supplied by Osaka Vacuum, Ltd., Japan) tandem was utilized to

achieve a background pressure of 10^{-5} Pa by evacuating the air from the sputtering chamber. An injection of high-purity gas of argon (Ar), supplied by Iwatani Industrial Gases Corporation, was regulated at a fixed flow rate of 15 sccm using an Ar mass flow meter (3660 series supplied by Kojima Instruments Inc.) to acquire a deposition pressure of 1.33×10^{-1} Pa. Afterward, the Si wafer substrate was regulated at 600 °C from behind by the heater with a digital temperature regulator (E5CN supplied by OMRON Corporation). Throughout the β -FeSi₂ film-coating process, the substrate temperature was preserved at this value. For the sputtering, the V value of 1 kV was applied from an HD1K-30 N direct-current power source supplied by Micro Denshi Co., Ltd. Saitama, Japan, and the generated sputtering current fixed at 1.5 mA. The time period of the sputtering process was set at 24 h. The thickness of the constructed β -FeSi₂ film was estimated to be about 300 nm. The technical parameters used in the creation process of n - β -FeSi₂/ p -Si heterojunctions are presented in Table 1.

2.2. Fabrication of metallic contacts

Prior to the fabrication of Ohmic contacts, the native oxide layer on the manufactured heterojunctions was cleansed by a 1% diluted HF acid solution. Afterward, the DI water was used to rinse the remaining HF solution, then dried using N₂ gas. The front and back Ohmic electrodes were constructed at an ambient temperature through magnetron sputtering with an RF power source (Cesar-133 supplied by Dressler Cesar). The palladium (Pd) Ohmic electrode was applied to the Si side using a Pd target with 4 N purity, and the aluminum (Al) Ohmic electrode constructed on the β -FeSi₂ side using an Al target with 4 N purity. The completed heterojunction device was around 1.0 mm² in area. There is no post-annealing treatment on the metallic contacts when used with the heterojunctions. The technical parameters used in the creation of Pd and Al electrodes are summarized in Table 2. A schematic of the constructed n - β -FeSi₂/ p -Si heterojunctions is presented below:

The quality of Al and Pd electrodes was demonstrated using I - V characteristics, separately measured at each side of the Ohmic contact (see Fig. 1). Fig. 2 reveals the I - V curve of the Al/ β -FeSi₂ and Pd/ p -Si Ohmic contact. The results for both Ohmic contacts show a straight line with very low current values, proving that the Pd and Al electrodes were properly created [18].

In this study, both sides made Ohmic contact, ideally to allow the current to pass from both sides of the β -FeSi₂/Si heterojunction devices. To form the Ohmic contact between the metal and semiconductor, the important parameters to take into consideration are work function (φ_M), electron affinity (χ), and barrier height (φ_B) as depicted in the following equations [41]:

$$\varphi_{B_n} = \varphi_M - \chi; \text{ for } n\text{-type semiconductor} \quad (1)$$

$$\varphi_{B_p} = \frac{E_g}{q} + (\chi - \varphi_M); \text{ for } p\text{-type semiconductor} \quad (2)$$

For p -type semiconductors, the φ_M of metal should exceed χ of the semiconductor to allow the electron to pass the interface [41]. Conversely, n -type semiconductor/metal Ohmic contact forms when the

Table 1

The technical parameters used in the creation process of n - β -FeSi₂/ p -Si heterojunctions.

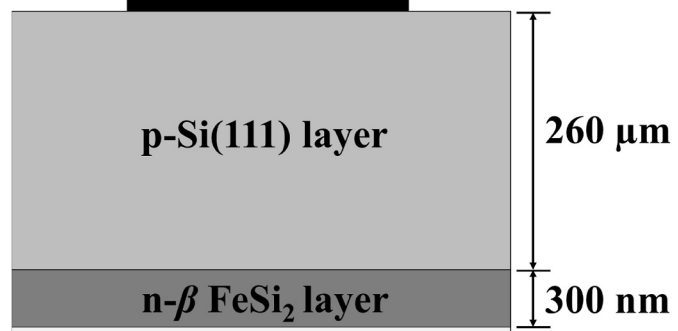
Sputtering target	FeSi ₂ (purity: 4 N)
Substrate temperature	600 °C
Base pressure	1×10^{-5} Pa
Operating pressure	1.33×10^{-1} Pa
Ar gas flow rate	15 sccm
Sputtering rate	0.15 nm/min
Discharge voltage	950 V
Discharge current	1.2 mA
Film thickness	300 nm

Table 2

Technical parameters used in the creation of Pd and Al electrodes.

	Pd contact	Al contact
Sputtering target	Pd (purity: 4 N)	Al (purity: 4 N)
Substrate temperature	Room temperature	Room temperature
Base pressure	1×10^{-5} Pa	1×10^{-5} Pa
Operating pressure	1.33×10^{-1} Pa	2.66×10^{-1} Pa
Ar gas flow rate	10 sccm	10 sccm
Discharge power	200 W	200 W
Sputtering rate	8.3 nm/min	4.2 nm/min
Film thickness	500 nm	500 nm

Pd ohmic contact



Al ohmic contact

Fig. 1. Schematic for our heterostructures constructed by DCS with faceted targets.

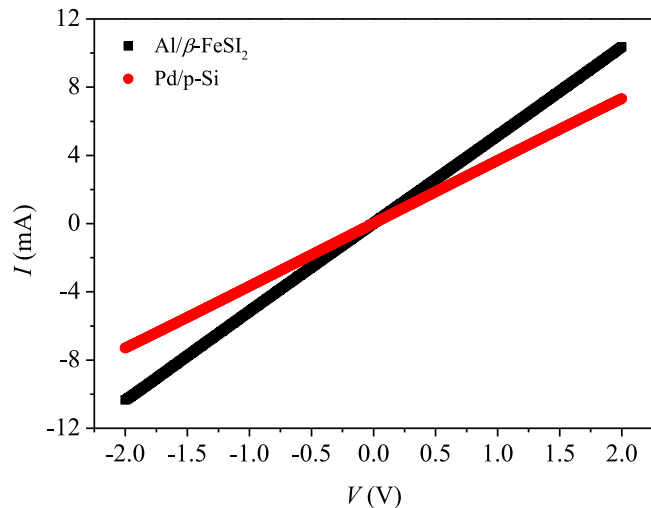


Fig. 2. The I - V measurements of the Al/ β -FeSi₂ and Pd/ p -Si Ohmic contacts.

φ_M of metal is close to or lower than χ of the semiconductor [41]. In any case, the φ_B of Ohmic contact should be minimized to reduce resistance across the contact [41]. Hence, Pd was applied on the Si side due to its φ_M of 5.12 which is higher than χ of 4.05 eV of p -type Si [42,43]. Meanwhile, Al with φ_M of 4.10 eV is the closest possible value to χ of 4.16 eV for n -type β -FeSi₂ among other conventional metal electrodes [43,44].

2.3. Characterizations of the built β -FeSi₂ thin films and n- β -FeSi₂/p-Si heterojunctions

The Field-Emission Scanning Electron Microscopy (FESEM) technique was utilized to provide the surface topography of the β -FeSi₂ films. Surface characterization was executed using an FESEM (Carl Zeiss Co., Ltd.) at 50kx magnification with an accelerating voltage of 3 kV for top view and 5 kV for side view. An FESEM (S-4700 Hitachi High-Technologies Corporation) was applied with the acceleration V of 5 kV and a magnification of 50 k times to observe the β -FeSi₂/Si layer on a cross-sectional structure. The β -FeSi₂ film orientation, as well as the epitaxial creation of β -FeSi₂ on the 111-oriented Si wafers, were analyzed through the XRD measurement apparatus (RINT2000/PC) utilization of a 2 θ - θ mode measuring between 20 and 70° including the pole figure mode. The AC variant of impedance spectroscopy was utilized to record the Z' and Z'' data. To examine the Z' and Z'' profiles, an LCR Meter (E4980A Precision Agilent Technologies, Inc.) was used to supply the frequency values ranging from 20 Hz to 2 MHz and the different V from -1 V to 1 V. This impedance measurement was carried out under darkness at room temperature. The equivalent circuit model of the constructed heterojunctions was derived from the Z'-Z' characteristics. Additionally, the simulation of circuit parameters was carried out via the employment of EC-Lab Software. The τ value of charge carriers was estimated utilizing the peak value of the Z''-f plot. The ϵ' , ϵ'' , and tan δ were originally calculated through the obtained Z''-Z' curves to study the behavior of the polarization and relaxation on the manufactured heterojunctions. For the parameters associated with the conduction process of the heterojunctions, the characteristics of σ_{AC} were extracted from the Z' and Z'' data, while the designation of σ_{DC} can be performed by the intercept of the y-coordinate drawn from a linear segment at a low f zone of the σ_{AC} -f spectrum. Also, the S factor and σ_{DC} can be appraised via fitting the σ_{AC} characteristics with the power law derived by Jonscher.

3. Experimental results and discussion

3.1. Fundamental parameters of n- β -FeSi₂/p-Si heterojunctions

In Fig. 3, the energy band diagram of the n- β -FeSi₂/p-Si heterojunctions is based on the parameters of Si and β -FeSi₂, reported throughout the years [45,46]. The β -FeSi₂ not only possesses a good built-in potential (V_{bi}) of 1.02 eV at 300 K but also a compromising valence band offset (ΔE_v) of 0.46 eV which obstructs the

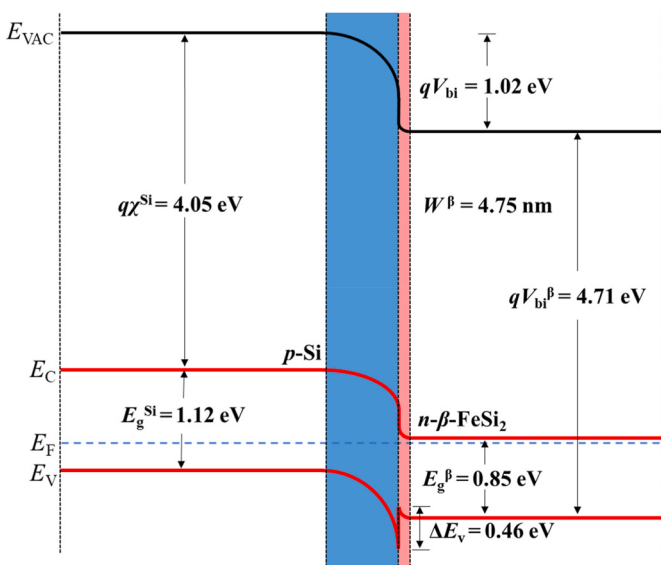


Fig. 3. Energy band diagram based on n- β -FeSi₂/p-Si heterojunctions.

photogeneration process [45]. The holes are still able to be transmitted to the Si side in practice due to the interface states originating from an imperfect interface [45]. The penetration from the tunneling effect is represented as a spike in band offset [45]. Due to their high carrier density and shallow donor level, the Fermi level of β -FeSi₂ should be located near the conduction band [45]. The Si side of n- β -FeSi₂/p-Si heterojunctions governs most of the depletion region of the heterojunction [45]. On the flip side, the width of the depletion region of β -FeSi₂ (W_β) is determined by this expression [47]:

$$W_\beta = \sqrt{\frac{2N_{si}\epsilon_{si}\epsilon_\beta(V_{bi} - V)}{qN_\beta(N_\beta\epsilon_\beta + N_{si}\epsilon_{si})}} \quad (3)$$

where ϵ_{si} is the permittivity of silicon with the value of 11.9 [46]. ϵ_β is the relative permittivity of FeSi₂ valued at 31 [46]. q is a charge constant of 1.602×10^{-19} C. N_{si} and N_β is the carrier concentration of Si (1.5×10^{15} cm⁻³) and β -FeSi₂ (1.0×10^{17} cm⁻³), respectively [18]. The W_β at $V = 0$ V was found to be 4.754 nm.

Previously, we estimated the interface state density (N_{ss}) of n- β -FeSi₂/p-Si heterojunctions and studied its characteristics at different f values from the extraction of the measured capacitance-voltage-frequency (C-V-f) and conductance-voltage-frequency (G/ω-V-f) under darkness [18]. The value of N_{ss} was computed by the Hill-Coleman and Nicollian-Brews approaches as follows [18]:

$$N_{ss} = \frac{2}{qA} \left(\frac{(G_m/\omega)_{max}}{(1 - C_m/C_{ox})^2 + ((G_m/\omega)_{max}/C_{ox})^2} \right) \quad (4)$$

where ω is the angular frequency and A is the junction area (0.1 cm²), $(G_m/\omega)_{max}$ is the maximum measured conductance value and C_m is C corresponding to $(G_m/\omega)_{max}$. C_{ox} is the capacitance of the insulator layer.

Based on the estimation, the values of N_{ss} were 4.68×10^{11} eV⁻¹ cm⁻² at 1 MHz and 3.48×10^{12} eV⁻¹ cm⁻² at 5 kHz. The existing N_{ss} at the interface of n- β -FeSi₂/p-Si heterojunctions behaves as the source of leakage current and a trap center for photo-generated carriers, leading to degradation in the device's performance [18].

3.2. Examination of surface and cross-sectional view photographs

As can be observed from Fig. 4a, the surface images of the β -FeSi₂ films possess abundant grain boundaries with occasionally porous edges, which might act as a trap center for the excited charge carriers after being exposed to the light [16,17]. The presence of a trap center reduced the performance of the coated β -FeSi₂ films during NIR light detection [16,17]. The cross-sectional view of the β -FeSi₂ films and Si wafer layer in Fig. 4b shows a film thickness of about 300 nm and the observation of a clean junction without visible deformation. This seamless construction of the films is due to the DCS having a couple of facing targets. Contrary to the DC magnetron sputtering containing the target for sputtering parallel to a substrate holder, the substrate holder is positioned away from the facing targets for sputtering [14]. As a result, the high-energy electrons inside a vacuum chamber are confined to vertically expanding against the targets for sputtering by the magnetic field [14,15]. Afterward, the ionization of the sputtering gas is augmented, resulting in a sputtering rate rise and permitting a high rate of film construction [14,15]. Hence, DCS along with a couple of facing targets is characterized by the superior kinetic energy of impacted particles, superior plasma density, minor detrimental impact on film, and less increment in substrate temperature [15].

3.3. Structural examination

The XRD spectrum presented in Fig. 5 possesses two diffraction peaks of the intense (202)/(220) plane at 29.15° and weak (404)/(440) plane at 61.43°, which are identifiable to the epitaxially constructed β -FeSi₂

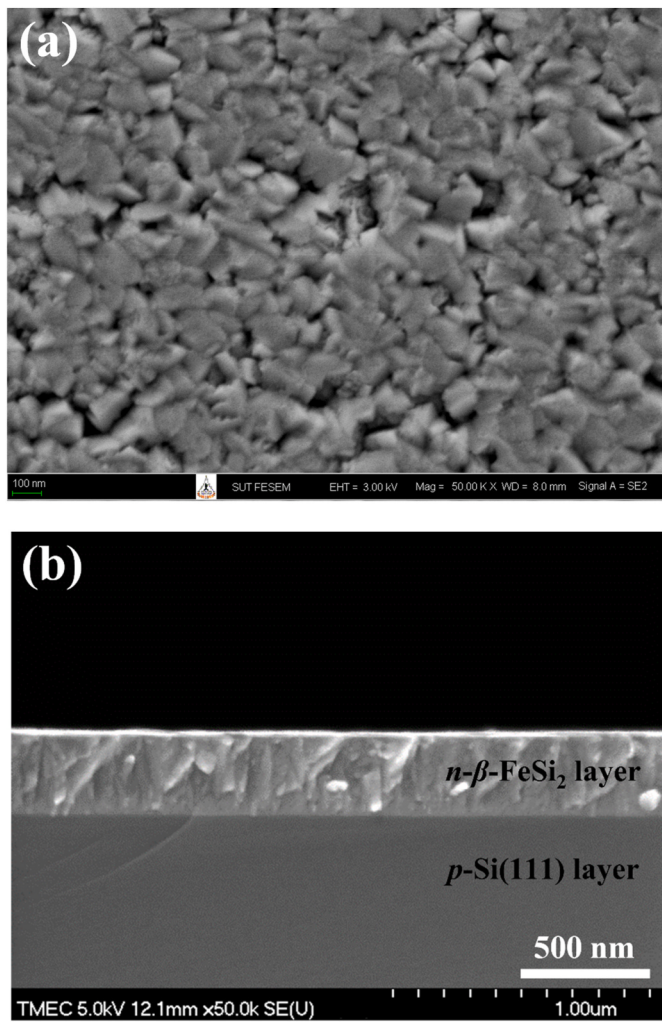


Fig. 4. FESEM images for our coated $n\text{-}\beta\text{-FeSi}_2$ layer on the surface of $p\text{-Si}$ wafer substrate observed at (a) top and (b) cross-section modes.

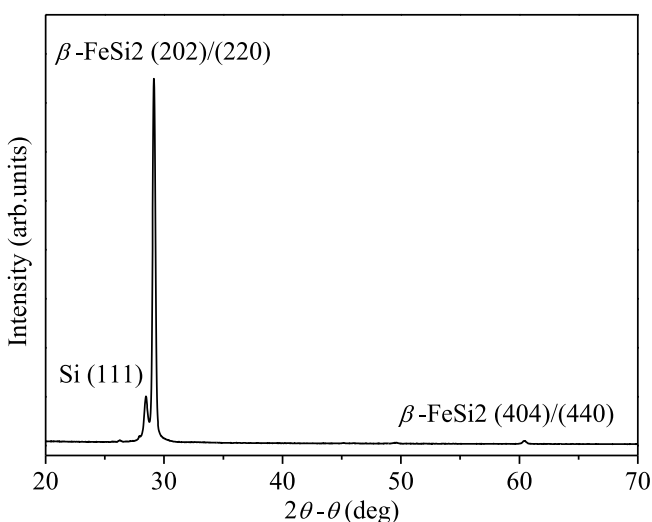


Fig. 5. Typical XRD line of the layer of $\beta\text{-FeSi}_2$ films forming onto the whole surface of the Si substrate layer collected in the $2\theta - \theta$ scan mode.

films [16,17]. Additionally, another peak is located at 28.46° , implying Si substrates with the (111) orientation [16,17]. The acquired spectrum of $\beta\text{-FeSi}_2$ correlates with the JCPDS card numbered 04-007-1080. The crystallite size of the constructed $\beta\text{-FeSi}_2$ layer is roughly 32.45 nm through Eq. (5) known as Debye-Scherrer equation [48]:

$$D = \frac{\lambda \times 0.94}{\cos \theta \times \text{FWHM}} \quad (5)$$

Where D is the average diameter of the crystallite and λ refers to the 1.542 \AA wavelength generated from X-ray radiation of the $\text{CuK}\alpha$ source. Meanwhile, FWHM refers to the full width at half the maximum dominant peak of the XRD line in a unit of radian, while θ is the diffraction angle of XRD in a unit of radian.

Fig. 6 illustrates the pole figure obtained for the $\beta\text{-FeSi}_2$ 404/440 diffraction peak of our device. It can be clearly seen that the obtained pattern depicts the existence of three sorts of epitaxial variants. Specifically, the angle of rotation is 120° from one to another [18].

3.4. Characterization of impedance properties when changing the applied voltages

In this scenario, the charge portage and relaxation phenomena can be perceived through impedance spectroscopy [23,24]. Also, the prediction of an equivalent circuit model corresponding to the nature of heterojunction and its parameters can be implemented employing the $Z''\text{-}Z'$ data [20,21]. Under intensive study, the f dependence of electrical features for a device can be demonstrated in terms of $Z(\omega)$, which is composed of the Z' and Z'' components. The Z term can be interpreted according to the following formula [49,50]:

$$Z(\omega) = Z' + iZ'' \quad (6)$$

Here, ω specifies the angular frequency ($\omega = 2\pi f$), in which f conveys the bias frequency. Z' and Z'' refer to the real and imaginary components of the $Z(\omega)$, respectively, while i indicates the imaginary determinant, which equals $-1^{1/2}$.

Fig. 7a exhibits the outcome of Z' versus f characteristics for the constructed heterojunctions recorded under biasing diverse V values. According to the $Z'\text{-}f$ characteristics, two flat areas can be observed in the

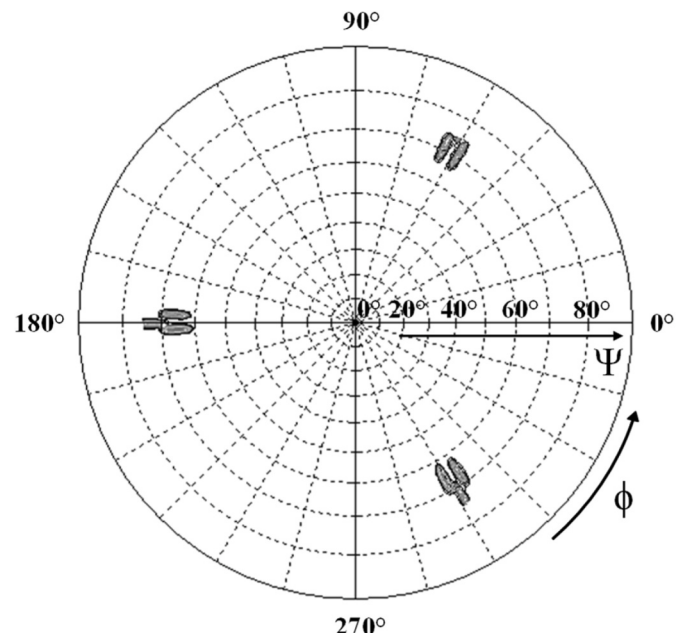


Fig. 6. The pole figure pattern of our $\beta\text{-FeSi}_2$ film layer created on the 111-oriented Si wafers.

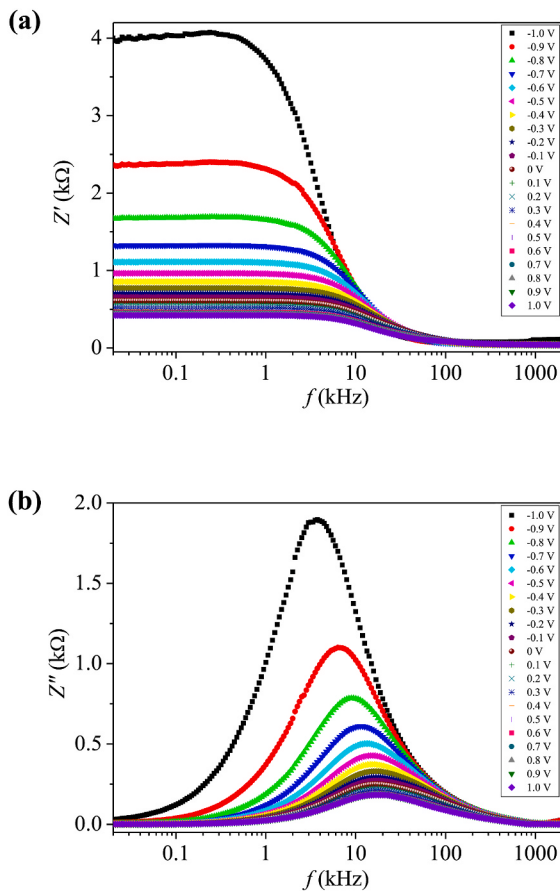


Fig. 7. (a) the plots between Z' and f and (b) the curves of $Z''-f$ in our constructed heterojunctions for different values of applied V .

low and high f range. A gradual attenuation of experimental Z' occurred when the V value was augmented under low f values. After the f was over 10 kHz, the Z' term seemed to be unaffected by the rising V values. This may be related to the space charge release in the material [23]. Moreover, these consequences of Z' can be specified as potentially originating in the resistances occurring from biasing the different f values [51,52]. For the high f regime, the term of Z' may rely on R_s derived from the Ohmic electrodes and the bulk resistance of the active layer [44,45]. In the zone of applied low f , the Z' part might correspond to parallel resistances (R_p), controlled through charge portage resistance [51,52].

Fig. 7b exhibits the characteristic curve of Z'' in relation to f for the fabricated heterojunctions under different applied V . The characteristic curve of $Z''-f$ exhibits peak behavior for each bias V at the dispersion zone of Z' . The magnitude of Z'' peak decreased with increasing V , and the Z'' peak shifted slightly toward the high f values. Based on the results presented in Fig. 7b, the paramount Z'' point was 1.90 kΩ at -1 V. In contrast, the peak of Z'' at 1 V was around 179.35 Ω. This feature pointed toward the electrical relaxation phenomenon within the fabricated heterojunctions relying on the alteration of V , and the τ value of the charge carriers mitigated with increasing V [53]. For all applied V values, the peak revealed considerable extension in an asymmetric pattern, pointing to the non-Debye type arising from the distribution of τ range determined by the peak width [54]. At low f , an increase in the Z'' magnitude was observed with the augmentation of the f value and V value. After the value of Z'' increased to the paramount point, the rise in the added f diminished the magnitude of Z'' . Nonetheless, the characteristic curve of $Z''-f$ for all V values stagnated at high f ($f > 100$ kHz), ascribable to the accumulation or occurrence of space charge polarization at a high f [51]. This behavior originated in the electrons from the β -FeSi₂ side, transferred into the space charge zone in the Si layer [51,

55].

Each peak of $Z''-f$ characteristics is related to a relaxation frequency (f_{\max}), referring to the electrical phenomena stemming from the device material [23]. Besides, the extracted f_{\max} value is related to the τ value, which can be specified from the following relationship [25]:

$$\tau = 1/\omega_{\max} = 1/2\pi f_{\max} \quad (7)$$

Here, τ means the carrier relaxation time, while ω_{\max} and f_{\max} signify the maximum angular relaxation frequency and the maximum relaxation frequency, respectively.

The variance of τ versus V of the manufactured heterojunctions is depicted in Fig. 8. A comparison of the τ value for all V variants revealed the highest value of 4.22×10^{-5} s at -1 V, and the smallest value of 6.69×10^{-6} s at 1 V. The τ of the mobile charge carriers relaxed with the augmentation of V levels [55]. The relaxation mechanism is designated to be involved with the plausible release of the space charge, with the electron rapidly charged and discharged at the interface of the junction between n - β -FeSi₂ films and p -Si wafer within the heterojunctions at the higher V value [52]. Consequently, the decline of τ value specified exciton generations at the interface zone of n - β -FeSi₂/ p -Si heterojunction, including the prompt transport of the charge carrier in the active layer [52].

Fig. 9 represents the characteristic curves of the $Z''-Z'$ plot for the manufactured heterojunctions. The experimental $Z''-Z'$ characteristic curves for each biased V value contain a single semicircular arc, validating that only a single kind of relaxation process exists in the manufactured heterojunctions at each V value [52]. With the augmentation of the biased V , the semicircle's magnitude was reduced, ascribable to the reduction of resistance originating in charge portage [54], inducing a rise in the activated conduction process [54]. All acquired $Z''-Z'$ were depressed semicircular arcs with center points situated beneath the Z' coordinate rather than on the Z' coordinate due to the width of the dispersion region of τ [34]. These distinct characteristics could be explained through an equivalent circuit model associated with the heterojunction behavior. The proper circuit model was shown on the inset of Fig. 9. The R_s models the series resistance arising from the Ohmic losses at contacts and electrodes, together with the bulk in the active layer [56,57]. Meanwhile, R_g , R_{gb} , and R_j are variants of R_p correspondingly defined by charge transfer resistance within the devices at grain, grain boundary, and junction [58–60]. The CPE_g , CPE_{gb} , and CPE_j parameters represent the non-ideal capacitance used to compensate for the deficiency of specific devices at grain, grain boundary, and junction

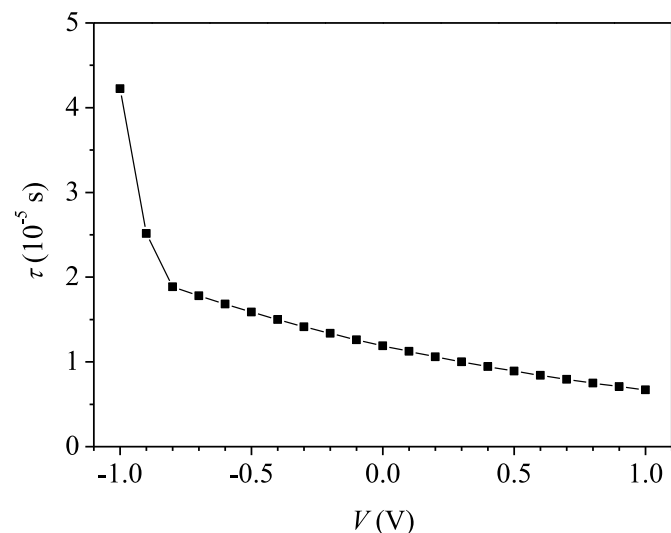


Fig. 8. Variation of estimated τ value with biased V value for the manufactured heterojunctions.

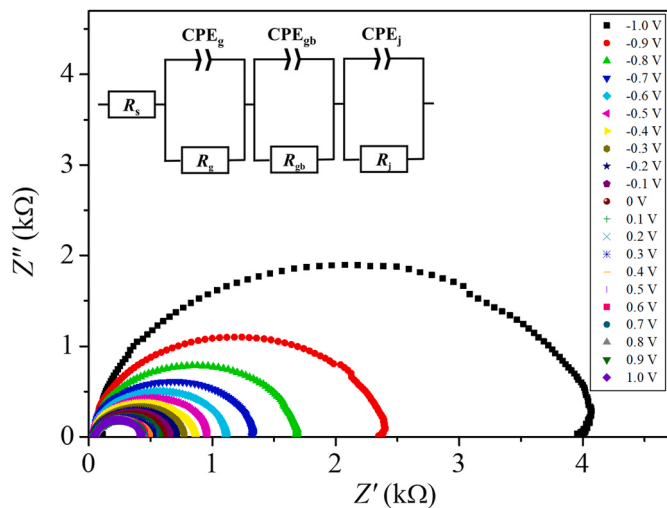


Fig. 9. Room temperature Z' - Z'' characteristic curves of the manufactured heterojunctions monitored by changing the applied V . The inserted graphic manifests the equivalent circuit model containing R_s in series with multiple parallel connections between R_p and CPE.

[56,57]. The electrical impedance correlated with CPE could be formulated according to the following equation [25]:

$$Z_{\text{CPE}}(\omega) = \frac{1}{(i\omega)^n \text{CPE}} \quad (8)$$

Here, n specifies a deviation in CPE from the ideal behavior of the capacitor, with the value of n being between 0 and 1. In the case of $n = 1$, CPE can be deemed an ideal capacitor.

Table 3 displays the values for equivalent circuit parameters extracted through the simulation by EC-Lab Software. In the event of R_s value, the R_s showed diminution with the elevation of bias V , which might be attributable to the rise in conductivity or reduction in contact resistance due to higher charge carrier transportability [61]. The results of R_g , R_{gb} , and R_j demonstrated a downward trend with the increment of V . This outcome might occur from the rise in electron momentum, enhancing the charge carriage mechanism [52] as well as the expansion of current density leading to carrier recombination [37–39]. The n values for the CPE_g, CPE_{gb}, and CPE_j components were close to 1 in the entire V range. Therefore, the CPE characteristics may behave as

capacitance [57,62]. The increasing trend of CPE should originate in the lessening of the depletion zone, in addition to the charge carriers accumulated within the active layer/charge transport layer interface [19,20] and the improved conductivity in the manufactured heterojunctions as augmenting V [23]. All simulated circuit parameters and their relations with biased V are expressed in Fig. 10a-10d.

3.5. Characterization of dielectric properties when changing the applied voltages

To study the polarization and relaxation of any material, it is necessary to calculate the part of $\epsilon(\omega)$, using the parts of $Z(\omega)$. The relationship between the real and imaginary parts of $\epsilon(\omega)$, as well as $Z(\omega)$, can be given by Eq. (9) [30]:

$$\frac{Z''}{(Z')^2 + (Z'')^2} \times \frac{1}{C_0\omega} = \epsilon'', \quad \frac{-Z''}{(Z')^2 + (Z'')^2} \times \frac{1}{C_0\omega} = \epsilon'. \quad (9)$$

where C_0 is the vacuum capacity obtained from the $\epsilon_0 E/t$, here, ϵ_0 refers to permittivity in the vacuum of 8.85×10^{-12} F per meter, E refers to the area of the electrode and t refers to film thickness.

In Fig. 11a, ϵ' curves are shaped as a plateau with a mostly flat peak in the f region below 10^4 Hz. The values of ϵ' under the influence of 100 Hz f were 890.63 and 441.98 at biased V of 1 V and -1 V, respectively. When the f approached the region beyond 10^4 Hz, the magnitude of the curves noticeably dropped with a rise in the f . The magnitude of ϵ' curves is related to the material's polarization [63,64]. In Fig. 11b, the value of ϵ'' shows f dependency on each V , with the magnitude of the curve decreasing as the f rises until it becomes flat and independent of the applied f at high f . The ϵ'' of individual material generally represents the dielectric losses from the bound charge relaxation phenomena which are comparable to the loss due to charge conduction [63,64]. The ϵ'' values of the heterojunctions are higher than ϵ' values and increase as the V rises. The origin of the high ϵ' and ϵ'' values may refer to Maxwell-Wagner relaxation behavior [65–67]. Space charge polarization occurs in materials with high grain conductivity and high grain boundary resistivity [65–67]. The polarization depends on the accumulation of the charge carriers trapped within the grain boundary resistivity during the carrier conduction process [65–67]. Hence, the ϵ' possesses a high value at low frequency. As the frequency rises, the grain boundary is unable to retain the charges induced by high electrical signals, resulting in space charge relaxation and a decrease in the ϵ' value [65–67]. Consequently, the energy lost during charge conduction will also be reflected in the high ϵ'' value [65–67]. At a higher f signal, the

Table 3

Fitted parameters for the equivalent circuit of the heterojunctions simulated via EC-Lab Software.

V (V)	R_s (Ω)	R_g (Ω)	R_{gb} (Ω)	R_j (Ω)	CPE _g (nF)	n	CPE _{gb} (nF)	n	CPE _j (nF)	n
-1.0	84.16	1467.00	428.00	2101.00	11.84	1.00	43.60	0.97	4.84	0.99
-0.9	75.99	798.00	267.50	1279.00	12.20	0.95	43.70	0.95	4.94	0.99
-0.8	65.20	476.31	211.04	961.06	12.63	0.97	43.78	1.00	5.00	1.00
-0.7	58.60	364.09	182.06	736.52	13.00	0.97	44.44	1.00	5.04	1.00
-0.6	55.50	321.64	151.45	582.80	13.89	1.00	45.28	1.00	5.10	1.00
-0.5	53.27	292.31	127.69	487.03	15.87	1.00	47.62	1.00	5.26	1.00
-0.4	51.83	267.07	108.18	420.65	18.60	0.99	51.67	1.00	5.56	1.00
-0.3	50.58	239.13	94.93	380.87	22.30	1.00	57.61	1.00	6.35	1.00
-0.2	49.52	229.46	82.44	351.16	26.95	1.00	65.80	1.00	7.44	0.99
-0.1	48.60	208.72	70.60	323.08	32.35	0.95	76.90	1.00	8.92	0.97
0	47.72	196.37	62.84	296.44	38.63	0.94	82.31	1.00	9.54	0.98
0.1	46.97	184.85	57.30	280.97	42.35	0.97	84.70	1.00	10.78	0.97
0.2	46.34	175.07	53.96	270.55	44.60	0.98	90.92	1.00	11.49	0.97
0.3	45.99	164.75	50.06	260.33	47.98	0.96	95.96	1.00	11.99	0.97
0.4	45.50	156.85	47.96	249.15	53.95	0.93	107.90	1.00	12.98	0.95
0.5	45.20	150.92	45.15	241.44	58.43	0.94	116.86	0.99	14.48	0.96
0.6	45.10	144.95	43.65	232.21	60.23	0.95	124.46	0.98	15.74	0.97
0.7	45.00	139.00	42.15	225.00	61.19	0.92	132.38	0.99	17.06	0.96
0.8	44.90	130.10	41.65	220.80	63.43	1.00	149.10	1.00	19.48	1.00
0.9	44.90	126.58	41.30	217.32	72.45	1.00	176.30	1.00	23.03	1.00
1.0	44.87	122.97	40.91	213.63	80.16	0.98	198.50	1.00	25.33	1.00

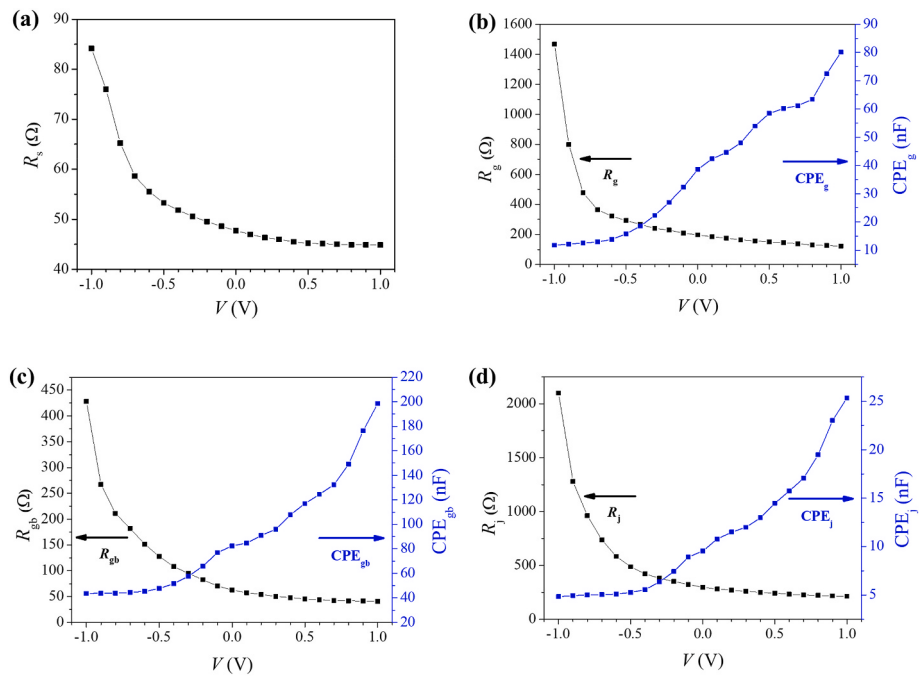


Fig. 10. Graph showing the variation in (a) R_s , (b) R_g - CPE_g , (c) R_{gb} - CPE_{gb} , and (d) R_j - CPE_j of the formed heterostructures biased with diverse V values.

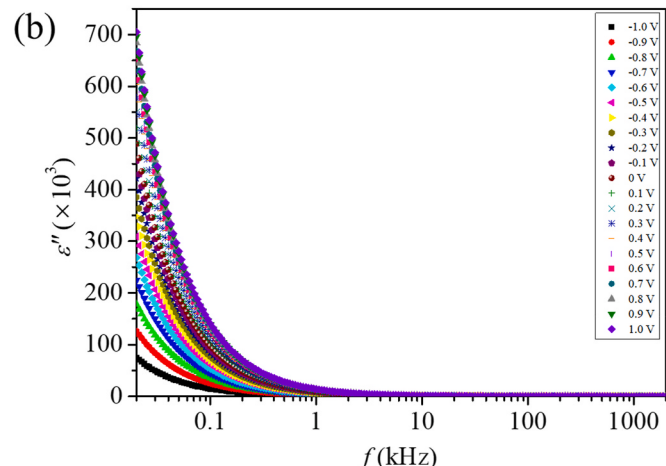
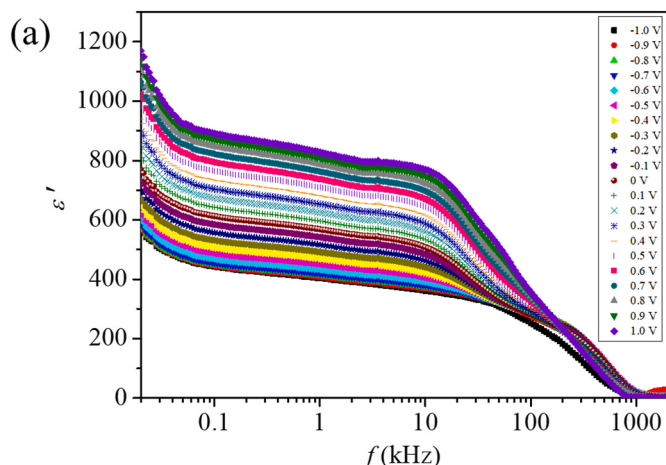


Fig. 11. Plots of (a) ϵ' and (b) ϵ'' against f at various V for the constructed heterojunctions.

charges could not achieve long-range transition, resulting in a decrease in the ϵ'' value with an increasing bias [30].

The $\tan \delta$ values associated with the loss originated from the energy used on mobile charge conduction and thermal degeneracy during dipole relaxation [30]. Utilizing the ϵ' and ϵ'' , the $\tan \delta$ could be derived from the proportion of the two variables depicted as $\tan \delta = \epsilon''/\epsilon'$ [63, 64]. In Fig. 12, the $\tan \delta$ - f curve at f lower than 10^4 Hz resembled the ϵ'' - f curve. Based on Maxwell-Wagner, space charge accumulation occurred, causing interfacial polarization at low f . The charge movement was changed by the heightened f , resulting in a magnitude decrease [65–67]. At an f higher than 10^5 Hz, the magnitude increases as raised f , reflecting the absorption that occurred during dipolar relaxation [66–68]. The $\tan \delta$ values of the heterojunctions presented high values indicating a leaky nature [69]. It should be noted that the constructed heterojunctions were less leaky compared to their nanocrystalline counterparts [25]. The accumulation of the interface states might be the main source of the

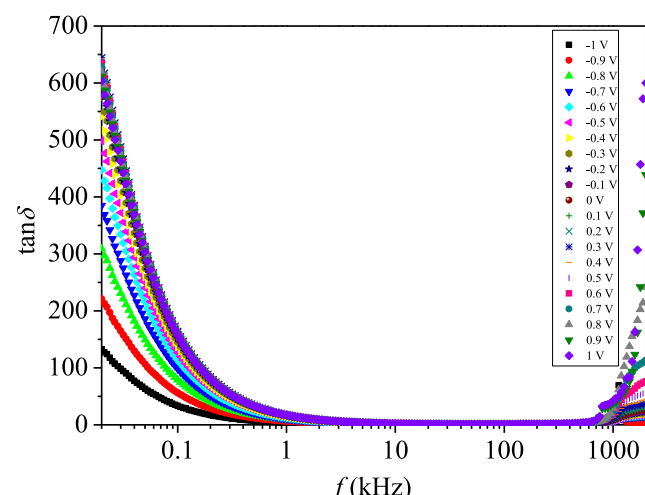


Fig. 12. Plots of the $\tan \delta$ and the $\log f$ at various biased V for the constructed heterojunctions.

inclinations in each dielectric parameter following the increasing biased V [26,27].

3.6. Characterization of conductive properties when changing the applied voltages

The σ_{AC} characteristics can be clarified utilizing the JRM concept based on the hopping movement induced by the separated mobile ions when the potential was adequate [54]. Besides, the process of jump relaxation is derived from the superposition of periodic lattice potential governed by the immobile ions and the cage-effect potential due to the repulsive Coulomb interaction of its neighboring mobile ions [54]. The augmentation of σ_{AC} as the f value increased may be ascribed to the bound carriers trapped in the junctions, while the free-charge carriers caused conductivity to diminish according to the rise in f [70,71].

The estimation of σ_{AC} for the heterojunctions can be achieved through the relationship expressed below [54]:

$$\sigma_{AC} = \frac{t}{E} \cdot \frac{Z'}{(Z')^2 + (Z'')^2} \quad (10)$$

Here, σ_{AC} refers to the AC conductivity, t means the film thickness, and E conveys the electrode's area, while Z' and Z'' indicate the real and imaginary components of $Z(\omega)$, respectively.

The σ_{AC} value for the manufactured heterojunctions evaluated by Eq. (10) was plotted over a biased f range with diverse V values between -1 V and 1 V, as revealed in Fig. 13. As can be clearly observed, an increase in σ_{AC} occurred following the augmenting f value. Therefore, the σ_{AC} behavior of the manufactured heterojunctions should be dominated by the bound carriers [70]. For each V in the flat zone at low f values, the σ_{AC} values were similar to those of the σ_{DC} extrapolated from the y-coordinate intercept of σ_{AC} versus f curve. This originates from the insufficiency of the electric field for the hopping conduction process of the charge carriers [54]. At a high f regime, the observation of the distribution zone of σ_{AC} originates in the ratio between the achievement and non-achievement of hopping based on the increasing f value [54]. The dispersion and feedback behavior of σ_{AC} to f can be expressed as the term $A\omega^S$ [54]. The increasing trend of σ_{AC} value along the elevating f was found when f was biased over the sufficient value. This sufficient f value is signified as the hopping frequency (f_H) [31], with f_H being in the range where the slope of the σ_{AC} versus f spectrum begins to change [31]. The f_H value for each specified V value can be designated from the universal law indicated below [34]:

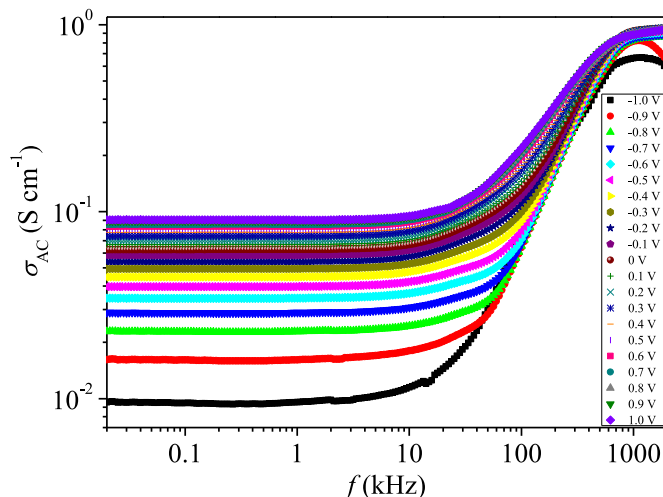


Fig. 13. Profile of σ_{AC} against f for the manufactured heterojunctions inspected as a function of the biased V value.

$$\left(\frac{\sigma_{DC}}{A}\right)^{\frac{1}{S}} = f_H \quad (11)$$

where σ_{DC} is the DC conductivity extracted from the characteristic of σ_{AC} against V at a low f regime, where the σ_{AC} values are f independent. A specifies the dispersion parameter, and S is the dimensionless exponent associated with the mobile ion-lattice interaction. Additionally, the f position corresponding to the σ_{AC} value equal to $2\sigma_{DC}$ can also be used to predict the f_H value [34].

Utilizing the power law developed by Jonscher, the raised trend in σ_{AC} augmenting the f value at the high f zone can be elucidated through the following relationship [71,72]:

$$\sigma_{AC} = \sigma_{DC} + A\omega^S \quad (12)$$

Using the S value, significant physical behavior can be explained. when $S \leq 1$, indicating translational motion where charge particles prefer a translational movement with abrupt hopping [54]. When S is over 1, it implies the localized hopping movement of carriers with short-range hopping between neighboring positions [54].

Based on the power of Jonscher's law, the augmentation of conductivity on increasing the f value can be clarified by the electric energy process in conjunction with the high f value [72,73]. This can productively carry forward the bound electric charge carriers [72,73].

The fitted S at different biased V for the constructed heterojunctions is presented in Table 4. The fitted result revealed S values higher than 1, ranging from 1.61 at -1 V to 1.23 at 1 V, indicating a short-range hopping of charge particles without leaving neighbor sites taking place in the constructed heterojunctions [54].

The fitting result of the σ_{DC} is plotted against the V value in Fig. 14a. The obtained σ_{DC} originated in the long-range translation of the induced particles, including the achieved hopping of charge carriers toward unoccupied neighboring situations [54]. The σ_{DC} value was projected to be 9.49×10^{-3} S cm $^{-1}$ with the reverse biased V of -1 V, while the value at 1 V of the σ_{DC} increased to 8.87×10^{-2} S cm $^{-1}$ as the charge carriers accumulated within the materials along with the increase in V [35].

4. Conclusion

The collection of AC impedance of n - β -FeSi $_2$ / p -Si heterojunctions was executed under various applied V values between -1 V and 1 V, including a wide gamut of f between 20 Hz and 2 MHz. All Z'' - Z' curves for all V values reveal single arc patterns with their curve centers

Table 4

The variance of σ_{DC} and S parameters fitted from the power of Jonscher's law under different V values.

V (V)	σ_{DC} (S cm $^{-1}$)	A	S
-1.0	9.49×10^{-3}	3.15×10^{-13}	1.61
-0.9	1.58×10^{-2}	3.56×10^{-13}	1.58
-0.8	2.22×10^{-2}	4.79×10^{-13}	1.55
-0.7	2.80×10^{-2}	7.91×10^{-13}	1.52
-0.6	3.35×10^{-2}	1.35×10^{-12}	1.48
-0.5	3.77×10^{-2}	2.29×10^{-12}	1.44
-0.4	4.39×10^{-2}	3.83×10^{-12}	1.41
-0.3	5.08×10^{-2}	4.84×10^{-12}	1.38
-0.2	5.53×10^{-2}	6.90×10^{-12}	1.37
-0.1	5.96×10^{-2}	8.77×10^{-12}	1.36
0	6.29×10^{-2}	1.53×10^{-11}	1.35
0.1	6.64×10^{-2}	2.01×10^{-11}	1.33
0.2	7.00×10^{-2}	2.29×10^{-11}	1.32
0.3	7.35×10^{-2}	2.9×10^{-11}	1.31
0.4	7.67×10^{-2}	3.27×10^{-11}	1.30
0.5	7.98×10^{-2}	3.91×10^{-11}	1.29
0.6	8.28×10^{-2}	3.94×10^{-11}	1.29
0.7	8.52×10^{-2}	4.23×10^{-11}	1.28
0.8	8.68×10^{-2}	5.71×10^{-11}	1.26
0.9	8.82×10^{-2}	7.22×10^{-11}	1.25
1.0	8.87×10^{-2}	8.75×10^{-11}	1.23

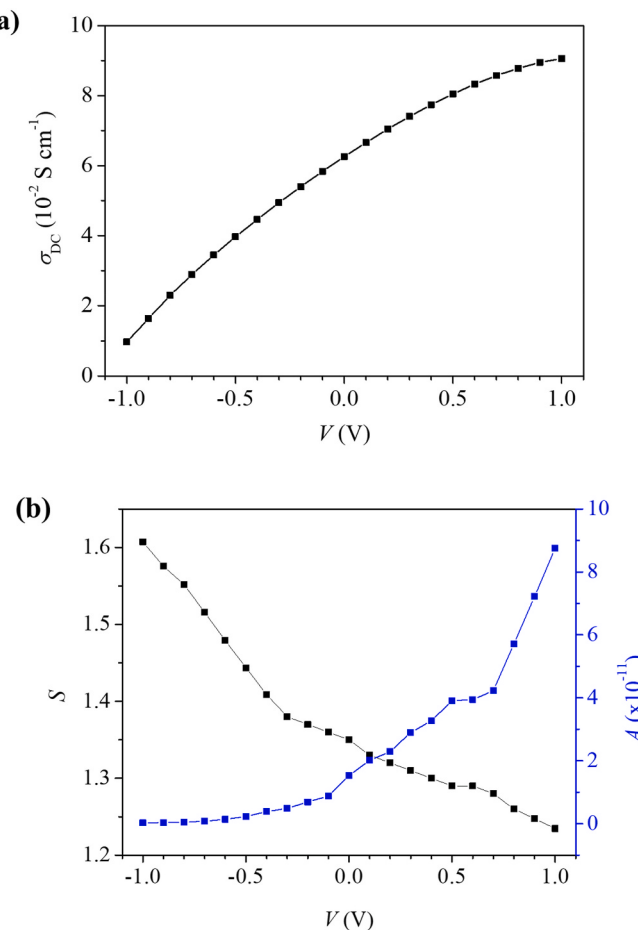


Fig. 14. The extracted (a) σ_{DC} and (b) S - A versus V relationship for the manufactured heterojunctions.

situated beneath the Z' axis. A semicircular arc specifies a single process of carrier relaxation. The reduction of τ signifies fast transportation of the charge carrier in the active layer. As the V values increased, it was noticeable that the semicircular arc diminished in size. For these reasons, the heterojunction conduct was equivalent to a circuit model comprising R_s in serial connection with multiple parallel circuits of R_p and CPE, representing grain, grain boundary, and junction. The R_s values were simulated to 84.16Ω and 44.87Ω at -1 V and 1 V , respectively. All estimated R_p values were also lower as the biased V increased, with all appraised CPE values being higher as the biased V increased. The values of ϵ' derived from the impedance results were reduced as the V increased. The plateau remained steady until the f passed the 10^4 Hz region, where the value gradually plummeted due to relaxation. The $\tan \delta$ - f plots were comparable to the ϵ'' - f plot but with a rising peak past the 10^5 Hz range. The heterojunctions were revealed to be quite leaky in response to reverse bias, albeit showing a better improvement from the nanocrystalline FeSi_2 device. Each σ_{AC} arranged per the usage of the Z'' - Z' data against the V profile discloses the flatland and distribution regimes at low and high f zones, respectively. The S values for all V values were between 1.61 and 1.23, indicating that the charge carrier transport was superintended by localized hopping movement between neighboring positions. The σ_{DC} value, obtained by the y-intercept from a straight line on the σ_{AC} - f graph at low f values, was elevated as V increased. The heightening of σ_{DC} should be relative to the augmentation for charge carriers when the V value was elevated to a higher value. The phenomena observed in this study provide the behavior of heterostructure and excess carrier which was the main culprit of leakage current in response to reverse bias.

CRediT authorship contribution statement

Nattakorn Borwornpornmetee: Writing – review & editing, Writing – original draft, Visualization, Methodology, Investigation, Formal analysis. **Rawiwan Chaleawpong:** Writing – review & editing, Writing – original draft, Visualization, Methodology, Investigation, Formal analysis. **Peerasil Charoenyuenyao:** Writing – review & editing, Investigation, Formal analysis. **Adison Nopparuchikun:** Writing – review & editing, Methodology. **Boonchoat Paosawatyanyong:** Writing – review & editing, Supervision. **Phongsaphak Sittimart:** Writing – review & editing, Methodology. **Tsuyoshi Yoshitake:** Writing – review & editing, Supervision. **Nathaporn Promros:** Writing – review & editing, Methodology, Investigation, Funding acquisition, Formal analysis, Conceptualization.

Declaration of competing interest

The authors declare that they have no known competing financial interests or personal relationships that could have appeared to influence the work reported in this paper.

Data availability

No data was used for the research described in the article.

Acknowledgments

This work is supported by King Mongkut's Institute of Technology Ladkrabang under the KMITL doctoral scholarship (contract number KDS 2022/006). The allowance for carrying out this research was provided by the Academic Research Fund, School of Science, King Mongkut's Institute of Technology Ladkrabang, with grant numbers 2562-01-05-29, 2562-01-05-44, and 2563-02-05-36. The authors also express their gratitude for the contribution and cooperation received from Research Unit of Integrated Science for Electronic, Material and Industry (ISEMI), School of Science, King Mongkut's Institute of Technology Ladkrabang.

Appendix A. Supplementary data

Supplementary data to this article can be found online at <https://doi.org/10.1016/j.mssp.2023.107671>.

References

- [1] M. Shaban, S. Izumi, K. Nomoto, T. Yoshitake, *n*-Type $\beta\text{-FeSi}_2$ /intrinsic-Si/*p*-type Si heterojunction photodiodes for near-infrared light detection at room temperature, *Appl. Phys. Lett.* 95 (2009), 162102, <https://doi.org/10.1063/1.3250171>.
- [2] N. Promros, R. Baba, M. Takahara, T.M. Mostafa, P. Sittimart, M. Shaban, T. Yoshitake, Epitaxial growth of $\beta\text{-FeSi}_2$ thin films on Si(111) substrates by radio frequency magnetron sputtering and their application to near-infrared photodetection, *Jpn. J. Appl. Phys.* 55 (2016), 06HC03, <https://doi.org/10.7567/JJAP.55.06HC03>.
- [3] M.K. Kolel-Veetil, T.M. Keller, Organometallic routes into the nanorealms of binary Fe-Si phases, *Materials* 3 (2010) 1049–1088, <https://doi.org/10.3390/ma3021049>.
- [4] J.E. Mahan, V.L. Thanh, J. Chevrier, I. Berbezier, J. Derrien, R.G. Long, Surface electron-diffraction patterns of $\beta\text{-FeSi}_2$ films epitaxially grown on silicon, *J. Appl. Phys.* 74 (1993) 1747–1761, <https://doi.org/10.1063/1.354804>.
- [5] T. Yoshitake, Y. Inokuchi, A. Yuri, K. Nagayama, Direct epitaxial growth of semiconducting $\beta\text{-FeSi}_2$ thin films on Si (111) by facing targets direct-current sputtering, *Appl. Phys. Lett.* 88 (2006), 182104, <https://doi.org/10.1063/1.2200153>.
- [6] P. Charoenyuenyao, R. Chaleawpong, N. Borwornpornmetee, B. Paosawatyanyong, P. Sittimart, T. Yoshitake, N. Promros, Investigation of morphological surface features, wetting behavior and mechanical traits under various substrate temperatures for beta iron disilicide prepared via facing-targets sputtering, *Mater. Sci. Semicond. Process.* 146 (2022), 106604, <https://doi.org/10.1016/j.mssp.2022.106604>.
- [7] J.E. Mahan, K.M. Geib, G.Y. Robinson, Epitaxial films of semiconducting FeSi_2 on (001) silicon, *Appl. Phys. Lett.* 56 (1990) 2126–2128, <https://doi.org/10.1063/1.103235>.

- [8] D.N. Leong, M.A. Harry, K.J. Reeson, K.P. Homewood, On the origin of the 1.5 μm luminescence in ion beam synthesized $\beta\text{-FeSi}_2$, *Appl. Phys. Lett.* 68 (1996) 1649–1650, <https://doi.org/10.1063/1.115893>.
- [9] M. Tanaka, Y. Kumagai, T. Suemasu, F. Hasegawa, Reactive deposition epitaxial growth of $\beta\text{-FeSi}_2$ layers on Si (001), *Appl. Surf. Sci.* 117/118 (1997) 303–307, [https://doi.org/10.1016/S0169-4332\(97\)80098-0](https://doi.org/10.1016/S0169-4332(97)80098-0).
- [10] M. Shaban, K. Nomoto, K. Nakashima, T. Yoshitake, Low-temperature annealing of *n*-type $\beta\text{-FeSi}_2$ /*p*-type Si heterojunctions, *Jpn. J. Appl. Phys.* 47 (2008) 3444, <https://doi.org/10.1143/JJAP.47.3444>.
- [11] S. Izumi, M. Shaban, N. Promros, K. Nomoto, T. Yoshitake, Near-infrared photodetection of $\beta\text{-FeSi}_2$ /Si heterojunction photodiodes at low temperatures, *Appl. Phys. Lett.* 102 (2013), 032107, <https://doi.org/10.1063/1.4789391>.
- [12] M. Shaban, K. Nakashima, T. Yoshitake, Substrate temperature dependence of photovoltaic properties of $\beta\text{-FeSi}_2$ /Si heterojunctions prepared by facing-target dc sputtering, *Jpn. J. Appl. Phys.* 46 (2007) 7708–7710, <https://doi.org/10.1143/JJAP.46.7708>.
- [13] T. Yoshitake, D. Nakaguchi, T. Ogawa, M. Itakura, N. Kuwano, Y. Tomokiyo, T. Kajiwara, K. Nagayama, Room-temperature epitaxial growth of ferromagnetic Fe₃Si films on Si(111) by facing target direct-current sputtering, *Appl. Phys. Lett.* 86 (2005), 26205, <https://doi.org/10.1063/1.1979894>.
- [14] C. Lin, D.C. Sun, S.L. Ming, E.Y. Jiang, Y.G. Liu, Magnetron facing target sputtering system for fabricating single-crystal films, *Thin Solid Films* 279 (1996) 49–52, [https://doi.org/10.1016/0040-6090\(95\)08124-0](https://doi.org/10.1016/0040-6090(95)08124-0).
- [15] S. Kim, K.H. Kim, Effect of magnetic field arrangement of facing targets sputtering (FTS) system on controlling plasma confinement, *Coatings* 10 (2020) 321, <https://doi.org/10.3390/coatings10040321>.
- [16] R. Chaleawpong, N. Promros, P. Charoenyuenyao, N. Borwornpormetee, P. Sittisart, P. Sittimart, Y. Tanaka, T. Yoshitake, Photovoltaic, capacitance-voltage, conductance-voltage, and electrical impedance characteristics of *p*-type silicon/intrinsic-silicon/*n*-type semiconducting iron disilicide heterostructures built via facing target direct-current sputtering, *Thin Solid Films* 709 (2020), 138229, <https://doi.org/10.1016/j.tsf.2020.138229>.
- [17] M. Shaban, K. Nomoto, S. Izumi, T. Yoshitake, Characterization of near-infrared *n*-type $\beta\text{-FeSi}_2$ /*p*-type Si heterojunction photodiodes at room temperature, *Appl. Phys. Lett.* 94 (2009), 222113, <https://doi.org/10.1063/1.3151915>.
- [18] R. Chaleawpong, N. Promros, P. Charoenyuenyao, A. Nopparuchikun, P. Sittimart, T. Nogami, T. Yoshitake, Production of *p*-type Si/*n*-type $\beta\text{-FeSi}_2$ heterojunctions using facing-targets direct-current sputtering and evaluation of their resistance and interface state density, *Phys. Status Solidi A* 215 (2018), 1701022, <https://doi.org/10.1002/pssa.201701022>.
- [19] S. Ali, S. Chang, M. Imran, Q. Shi, Y. Chen, H. Zhong, Impedance spectroscopy: a versatile technique to understand solution-processed optoelectronic devices, *Phys. Status Solidi RRL* 13 (2019), 1800580, <https://doi.org/10.1002/pssr.201800580>.
- [20] L. Xu, Y.-J. Lee, J.W.P. Hsua, Charge collection in bulk heterojunction organic photovoltaic devices: an impedance spectroscopy study, *Appl. Phys. Lett.* 105 (2014), 123904, <https://doi.org/10.1063/1.4896633>.
- [21] J. Panigrahi, Vandana, R. Singh, N. Batra, J. Gope, M. Sharma, P. Pathi, S. K. Srivastava, C.M.S. Rauthan, P.K. Singh, Impedance spectroscopy of crystalline silicon solar cell: observation of negative capacitance, *Sol. Energy* 136 (2016) 412–420, <https://doi.org/10.1016/j.solener.2016.06.041>.
- [22] A.F. Brana, E. Forniés, N. López, B.J. García, High efficiency Si solar cells characterization using impedance spectroscopy analysis, *J. Phys. Conf. Ser.* 647 (2015), 012069, <https://doi.org/10.1088/1742-6596/647/1/012069>.
- [23] A. Dey, J. Dhar, S. Sil, R. Jana, P.P. Ray, Bias voltage-dependent impedance spectroscopy analysis of hydrothermally synthesized ZnS nanoparticles, *J. Mater. Eng. Perform.* 27 (2018) 2727–2733, <https://doi.org/10.1007/s11665-018-3359-x>.
- [24] A. Buyukbas-Ulusun, İ. Taşçıoğlu, A. Tataroğlu, F. Yakuphanoglu, S. Altindal, A comparative study on the electrical and dielectric properties of Al/Cd-doped ZnO/*p*-Si structures, *J. Mater. Sci. Mater. Electron.* 30 (2019) 12122–12129, <https://doi.org/10.1007/s10854-019-01570-z>.
- [25] N. Borwornpormetee, R. Chaleawpong, P. Charoenyuenyao, A. Nopparuchikun, B. Paosawatyanong, P. Sittimart, T. Yoshitake, N. Promros, Reverse bias dependent impedance and dielectric properties of Al/*n*-NC Fe₃Si/*p*-Si/Pd heterostructures formed by facing-targets sputtering, *Mater. Sci. Semicond. Process.* 146 (2022), 106641, <https://doi.org/10.1016/j.mssp.2022.106641>.
- [26] T. Prakash, S. Ramasamy, B.S. Murty, Effect of DC bias on dielectric properties of nanocrystalline CuAlO₂, *Electron. Mater. Lett.* 9 (2013) 207–211, <https://doi.org/10.1007/s13391-012-2106-y>.
- [27] A. Kaya, Ö. Vural, H. Tecimer, S. Demirezen, Ş. Altindal, Frequency and voltage dependence of dielectric properties and electric modulus in Au/PVC + TCNQ/*p*-Si structure at room temperature, *Curr. Appl. Phys.* 14 (2014) 322–330, <https://doi.org/10.1016/j.cap.2013.12.005>.
- [28] B.M. Greenhoe, M.K. Hassan, J.S. Wiggins, K.A. Mauritz, Universal power law behavior of the AC conductivity versus frequency of agglomerate morphologies in conductive carbon nanotube-reinforced epoxy networks, *J. Polym. Sci. B Polym. Phys.* 54 (2016) 1918–1923, <https://doi.org/10.1002/polb.24121>.
- [29] P. Banerjee, N.S. Kumar, A. Franco Jr., A.K. Swain, K. Chandra Babu Naidu, Insights into the dielectric loss mechanism of biaxialotropic FeSi/SiC composite materials, *ACS Omega* 5 (2020) 25968–25972, <https://doi.org/10.1021/acsomega.0c03409>.
- [30] S. Sil, J. Datta, M. Das, R. Jana, S. Halder, A. Biswas, D. Sanyal, P.P. Ray, Bias dependent conduction and relaxation mechanism study of Cu₅FeS₄ film and its significance in signal transport network, *J. Mater. Sci. Mater. Electron.* 29 (2018) 5014–5024, <https://doi.org/10.1007/s10854-017-8463-4>.
- [31] M. Ahmad, M.A. Rafiq, Z. Imran, K. Rasool, R.N. Shahid, Y. Javed, M.M. Hasan, Charge conduction and relaxation in MoS₂ nanoflakes synthesized by simple solid state reaction, *J. Appl. Phys.* 114 (2013), 043710, <https://doi.org/10.1063/1.4816570>.
- [32] F. Yakuphanoglu, Y. Aydogdu, U. Schatzschneider, E. Rentschler, DC and AC conductivity and dielectric properties of the metal-radical compound: aqua [bis (2-dimethylaminomethyl-4-NIT-phenolato)] copper (II), *Solid State Commun.* 128 (2003) 63–67, [https://doi.org/10.1016/S0038-1098\(03\)00651-3](https://doi.org/10.1016/S0038-1098(03)00651-3).
- [33] M.E. Azim-Araghi, D. Campbell, Electrical conduction mechanisms in thermally evaporated thin films of 2-(4-biphenyl)-5-(4-tert-butylphenyl)-1, 3, 4-oxadiazole, *Thin Solid Films* 320 (1998) 320–323, [https://doi.org/10.1016/S0040-6090\(97\)00933-4](https://doi.org/10.1016/S0040-6090(97)00933-4).
- [34] P.S. Anantha, K. Hariharan, ac Conductivity analysis and dielectric relaxation behaviour of NaNO₃-Al₂O₃ composites, *Mater. Sci. Eng. B* 121 (2005) 12–19, <https://doi.org/10.1016/j.mseb.2004.12.005>.
- [35] N. Ben Messaoud, M. Braik, C. Dridi, M. Ben Ali, A. Ali, M.N. Abbas, A. Errachid, Optical, electrical and perchlorate sensing properties of a new CoPc derivative, *Sens. Lett.* 14 (2016) 928–937, <https://doi.org/10.1166/sl.2016.3713>.
- [36] J.C. Dyre, T.B. Schröder, Hopping models and ac universality, *Phys. Status Solidi B* 230 (2020) 5–13, [https://doi.org/10.1002/1521-3951\(200203\)230:1%3C5:AID-PSSB5%3E3.0.CO;2-J](https://doi.org/10.1002/1521-3951(200203)230:1%3C5:AID-PSSB5%3E3.0.CO;2-J).
- [37] D. Barreiro-Argüelles, G. Ramos-Ortiz, J.-L. Maldonado, E. Pérez-Gutiérrez, D. Romero-Borja, A. Álvarez-Fernández, PTB7:PC₇BM-based solar cells fabricated with the eutectic alloy field's metal as an alternative cathode and the influence of an electron extraction layer, *IEEE J. Photovoltaics* 7 (2016) 191–198, <https://doi.org/10.1109/JPHOTOV.2016.2617087>.
- [38] B. Qi, Z.-G. Zhang, J. Wang, Uncovering the role of cathode buffer layer in organic solar cells, *Sci. Rep.* 5 (2015) 7803, <https://doi.org/10.1038/srep07803>.
- [39] H. Wang, Y. Wang, B. He, W. Li, M. Sulaman, J. Xu, S. Yang, Y. Tang, B. Zou, Charge carrier conduction mechanism in PbS quantum dot solar cells: electrochemical impedance spectroscopy study, *ACS Appl. Mater. Interfaces* 8 (2016) 18526–18533, <https://doi.org/10.1021/acsami.6b03198>.
- [40] S. Demirezen, Frequency and voltage-dependent dielectric properties and electrical conductivity of Au/PVA (Bi-doped)/*n*-Si Schottky barrier diodes at room temperature, *Appl. Phys. A* 112 (2013) 827–833, <https://doi.org/10.1007/s00339-013-7605-7>.
- [41] S.M. Sze, Y. Li, K.K. Ng, *Physics of Semiconductor Devices*, fourth ed., John Wiley & sons, Hoboken, 2021.
- [42] D. Gu, S.K. Dey, P. Majhi, Effective work function of Pt, Pd, and Re on atomic layer deposited HfO₂, *Appl. Phys. Lett.* 89 (2006), 082907, <https://doi.org/10.1063/1.2336718>.
- [43] M.M.A. Moon, M.H. Ali, M.F. Rahman, J. Hossain, A.B.M. Ismail, Design and simulation of FeSi₂-based novel heterojunction solar cells for harnessing visible and near-infrared light, *Phys. Status Solidi A* 217 (2020), 1900921, <https://doi.org/10.1002/pssa.201900921>.
- [44] M. Shaban, A.M. Bayoumi, D. Farouk, M.B. Saleh, T. Yoshitake, Evaluation of photovoltaic properties of nanocrystalline-FeSi₂/Si heterojunctions, *Solid State Electron.* 123 (2016) 111–118, <https://doi.org/10.1016/j.sse.2016.05.006>.
- [45] M. Shaban, K. Nakashima, W. Yokoyama, T. Yoshitake, Photovoltaic properties of *n*-type $\beta\text{-FeSi}_2$ /*p*-type Si heterojunctions, *Jpn. J. Appl. Phys.* 46 (2007) L667, <https://doi.org/10.1143/JJAP.46.L667>.
- [46] J. Yuan, H. Shen, L. Lu, Influence of surface recombination and interface states on the performance of $\beta\text{-FeSi}_2$ -*c*-Si heterojunction solar cells, *Phys. B Condens. Matter* 406 (2011) 1733–1737, <https://doi.org/10.1016/j.physb.2011.02.017>.
- [47] S. Ohmagari, S. Al-Riyami, T. Yoshitake, Heterojunction diodes comprised of *n*-type silicon and *p*-type ultrananocrystalline diamond/hydrogenated amorphous carbon composite, *Jpn. J. Appl. Phys.* 50 (2011), 035101, <https://doi.org/10.1143/jjap.50.035101>.
- [48] P. Charoenyuenyao, N. Promros, R. Chaleawpong, N. Borwornpormetee, P. Sittisart, Y. Tanaka, T. Yoshitake, Impact of annealing temperature and carbon doping on the wetting and surface morphology of semiconducting iron disilicide formed via radio frequency magnetron sputtering, *Thin Solid Films* 709 (2020), 138248, <https://doi.org/10.1016/j.tsf.2020.138248>.
- [49] F.B. Bacha, S.M. Borchani, M. Damak, M. Megdiche, Optical and complex impedance analysis of double tungstates of mono- and trivalent metals for LiGd (WO₄)₂ compound, *J. Alloys Compd.* 712 (2017) 657–665, <https://doi.org/10.1016/j.jallcom.2017.04.107>.
- [50] R.K. Panda, D. Behera, Investigation of electric transport behavior of bulk CoFe₂O₄ by complex impedance spectroscopy, *J. Alloys Compd.* 587 (2014) 481–486, <https://doi.org/10.1016/j.jallcom.2013.10.195>.
- [51] A. Zkria, E. Abubakr, P. Sittimart, T. Yoshitake, Analysis of electrical characteristics of Pd/*n*-nanocarbon/*p*-Si heterojunction diodes: by C-V-*f* and G/*ω*-V-*f*, *J. Nanomater.* 2020 (2020), 4917946, <https://doi.org/10.1155/2020/4917946>.
- [52] Y. Zhang, L. Li, S. Yuan, G. Li, W. Zhang, Electrical properties of the interfaces in bulk heterojunction organic solar cells investigated by electrochemical impedance spectroscopy, *Electrochim. Acta* 109 (2013) 221–225, <https://doi.org/10.1016/j.electacta.2013.07.152>.
- [53] H. Zrida, K. Hriz, N. Jaballah, H. Hrichi, D. Kreher, M. Majdou, New soluble anthracene-based polymer for opto-electronic applications, *J. Mater. Sci.* 51 (2016) 680–693, <https://doi.org/10.1007/s10853-015-9037-6>.
- [54] S. Sila, M. Dasa, J. Dattaa, S. Haldera, P.P. Ray, Impedance spectroscopy study of hydrothermally synthesized nano-semiconducting bornite (Cu₅FeS₄), *Mater. Today: Proc.* 5 (2018) 9948–9957, <https://doi.org/10.1016/j.matpr.2017.10.192>.
- [55] L. Singh, I.W. Kim, W.S. Woo, B.C. Sin, H. Lee, Y. Lee, A novel low cost non-aqueous chemical route for giant dielectric constant CaCu₃Ti₄O₁₂ ceramic, *Solid*

- State Sci. 43 (2015) 35–45, <https://doi.org/10.1016/j.solidstatesciences.2015.03.018>.
- [56] B. Arredondo, M.B. Martín-López, B. Romero, R. Vergaz, P. Romero-Gomez, J. Martorell, Monitoring degradation mechanisms in PTB7:PC₇₁BM photovoltaic cells by means of impedance spectroscopy, Sol. Energy Mater. Sol. Cells 144 (2016) 422–428, <https://doi.org/10.1016/j.solmat.2015.09.050>.
- [57] A. Aouniti, H. Elmsellem, S. Tighadouini, M. Elazzouzi, S. Radi, A. Chetouani, B. Hammouti, A. Zarrouk, Schiff's base derived from 2-acetyl thiophene as corrosion inhibitor of steel in acidic medium, J. Taibah Univ. Sci. 10 (2016) 774–785, <https://doi.org/10.1016/j.jtusci.2015.11.008>.
- [58] M. Shaban, A. Zkria, T. Yoshitake, Temperature-dependent impedance spectra of nitrogen-doped ultrananocrystalline diamond films grown on Si substrates, IEEE Access 9 (2020) 896–904, <https://doi.org/10.1109/ACCESS.2020.3046969>.
- [59] N. Kavasoglu, C. Tozlu, O. Pakma, A.S. Kavasoglu, S. Ozden, B. Metin, O. Birgi, S. Oktik, Room-temperature interface state analysis of Au/Poly(4-vinyl phenol)/p-Si structure, Synth. Met. 159 (2009) 1880–1884, <https://doi.org/10.1016/j.synthmet.2009.06.015>.
- [60] M.M. Bülbül, S. Zeyrek, Ş. Altindal, H. Yüzer, On the profile of temperature dependent series resistance in Al/Si₃N₄/p-Si (MIS) Schottky diodes, Microelectron. Eng. 83 (2006) 577–581, <https://doi.org/10.1016/j.mee.2005.12.013>.
- [61] Y. Jiang, L. Pan, D. Wei, W. Li, S. Li, S.-E. Yang, Z. Shi, H. Guo, T. Xia, J. Zang, Y. Chen, The modified multi-step thermal annealing process for highly efficient MAPbI₃-based perovskite solar cells, Sol. Energy 174 (2018) 218–224, <https://doi.org/10.1016/j.solener.2018.09.016>.
- [62] N.O. Obi-Egbedi, I.B. Obot, M.I. El-Khaiary, Quantum chemical investigation and statistical analysis of the relationship between corrosion inhibition efficiency and molecular structure of xanthene and its derivatives on mild steel in sulphuric acid, J. Mol. Struct. 1002 (2011) 86–96, <https://doi.org/10.1016/j.molstruc.2011.07.003>.
- [63] H.H. Gullu, D.E. Yıldız, Capacitance, conductance, and dielectric characteristics of Al/TiO₂/Si diode, J. Mater. Sci. Mater. Electron. 32 (2021) 13549–13567, <https://doi.org/10.1007/s10854-021-05931-5>.
- [64] A. Kocigit, D.E. Yıldız, A. Sarilmaz, F. Ozel, M. Yıldırım, The dielectric performance of Au/CuCo₅S₈/p-Si heterojunction for various frequencies, J. Mater. Sci. Mater. Electron. 31 (2020) 22408–22416, <https://doi.org/10.1007/s10854-020-04742-4>.
- [65] X. Huang, H. Zhang, Y. Lai, J. Li, The lowered dielectric loss tangent and grain boundary effects in fluorine-doped calcium copper titanate ceramics, Appl. Phys. A 123 (2017) 1–7, <https://doi.org/10.1007/s00339-017-0947-9>.
- [66] S. Demirezen, S.A. Yerişkin, Frequency and voltage-dependent dielectric spectroscopy characterization of Al/(Coumarin-PVA)/p-Si structures, J. Mater. Sci. Mater. Electron. 32 (2021) 25339–25349, <https://doi.org/10.1007/s10854-021-06993-1>.
- [67] S. Karadaş, S.A. Yerişkin, M. Balbaşı, Y. Azizian-Kalandaragh, Complex dielectric, complex electric modulus, and electrical conductivity in Al/(Graphene-PVA)/p-Si (metal-polymer-semiconductor) structures, J. Phys. Chem. Solid. 148 (2021), 109740, <https://doi.org/10.1016/j.jpcs.2020.109740>.
- [68] M. Panda, A.K. Thakur, K. A. V. Srinivas, Thermal effects on the percolation behavior of polyvinylidene fluoride/nickel composites, J. Appl. Polym. Sci. 117 (2010) 3023–3028, <https://doi.org/10.1002/app.31223>.
- [69] H.H. Gullu, D.E. Yıldız, O. Surucu, M. Parlak, Frequency effect on electrical and dielectric characteristics of HfO₂-interlayered Si-based Schottky barrier diode, J. Mater. Sci. Mater. Electron. 31 (2020) 9394–9407, <https://doi.org/10.1007/s10854-020-03479-4>.
- [70] M.N. Kamalasan, N.D. Kumar, S. Chandra, Dielectric and ferroelectric properties of BaTiO₃ thin films grown by the sol-gel process, J. Appl. Phys. 74 (1993) 5679–5686, <https://doi.org/10.1063/1.354183>.
- [71] E.E. Tanrikulu, S.A. Yerişkin, On the changes in the dielectric, electric modulus, and ac electrical-conductivity in the Al/(C₂₉H₃₂O₁₇)/p-Si (MPS) structures in wide range of frequency and voltage, Phys. B Condens. Matter 623 (2021), 413345, <https://doi.org/10.1016/j.physb.2021.413345>.
- [72] A.K. Jonscher, Nature, the ‘universal’ dielectric response, Nature 267 (1977) 673–679, <https://doi.org/10.1038/267673a0>.
- [73] A. Barkhordari, H. Mashayekhi, P. Amiri, Ş. Altindal, Y. Azizian-Kalandaragh, On the investigation of frequency-dependent dielectric features in Schottky barrier diodes (SBDs) with polymer interfacial layer doped by graphene and ZnTiO₃ nanostructures, Appl. Phys. A 129 (2023) 1–11, <https://doi.org/10.1007/s00339-023-06539-8>.